REVIEW ARTICLE

Clinical photoacoustic imaging platforms

Wonseok Choi[1] · Eun-Yeong Park[1] · Seungwan Jeon[2] · Chulhong Kim[1,2]

Abstract

Photoacoustic imaging (PAI) is a new promising medical imaging technology available for diagnosing and assessing various pathologies. PAI complements existing imaging modalities by providing information not currently available for diagnosing, e.g., oxygenation level of the underlying tissue. Currently, researchers are translating PAI from benchside to bedside to make unique clinical advantages of PAI available for patient care. The requirements for a successful clinical PAI system are; deeper imaging depth, wider field of view, and faster scan time than the laboratory-level PAI systems. Currently, many research groups and companies are developing novel technologies for data acquisition/signal processing systems, detector geometry, and an acoustic sensor. In this review, we summarize state-of-the-art clinical PAI systems with three types of the imaging transducers: linear array transducer, curved linear array transducer, and volumetric array transducer. We will also discuss the limitations of the current PAI systems and describe latest techniques being developed to address these for further enhancing the image quality of PAI for successful clinical translation.

Keywords Photoacoustics · Optoacoustics · Medical imaging · Clinical systems · Ultrasound array transducer

1 Introduction

Photoacoustic imaging (PAI) based on the photoacoustic (PA) effect [1] is a rapidly growing biomedical imaging technique [2–10]. It reconstructs images from the captured ultrasound (US) signals generated from the materials that are thermally expanded by laser pulses [11–13]. Clinical advantages offered by the PAI systems are many, and we summarize some of them in the next paragraph.

Firstly, PAI provides high-contrast vascular images without using exogenous agents. It is commonly known that the contrast agents used for the conventional CT or MR angiography, such as iodixanol and iopamidol, could induce nephropathy leading to possible kidney failure [14].

Wonseok Choi, Eun-Yeong Park and Seungwan Jeon have contributed equally to this work.

✉ Chulhong Kim
  chulhong@postech.edu

[1] Department of Electrical Engineering, Pohang University of Science and Technology (POSTECH), 77 Cheongam-ro, Nam-gu, Pohang, Gyeongbuk, Republic of Korea

[2] Department of Creative IT Engineering, Pohang University of Science and Technology (POSTECH), 77 Cheongam-ro, Nam-gu, Pohang, Gyeongbuk, Republic of Korea

Considering that many vascular disease patients undergoing angiography also suffer from kidney diseases [15, 16], the use of agents may lead to the serious adverse effect on the patients' health [17]. The PAI system, on the other hand, uses hemoglobin itself as an endogenous agent since hemoglobin is a strong absorber of visible and near-infrared light. Thus, PAI can be a safe substitute for angiography technique avoiding the risks of adverse side effects. Secondly, PAI can distinguish chemical composition of biological tissue by utilizing the optical absorption spectra of different chromophores [18–21]. Since hemoglobin has different optical absorbance coefficients depending on whether it is bound or unbound to oxygen, PAI can give the oxygen saturation level of blood vessels by using multiple wavelengths [22]. Since tumors [23–28], vascular diseases [29, 30], and arthritis [31, 32] are known to cause abnormal changes in the surrounding microenvironment, such as neovascularization [33, 34], hypoxia [35], or ischemia [36], PAI is very useful for diagnosing them. Thirdly, since PAI is inherently compatible with US imaging, it provides anatomical information of the underlying tissue simultaneously with the PAI image for the better diagnosis of the underlying disease [37]. Other advantages of PAI include: PA images are more sensitive to small blood vessels than US Doppler images [29, 38], PA image has no speckle artifacts [39], and PAI system is

compact and affordable compared to the conventional tomography system such as CT and MRI. Currently, researchers are translating PAI from benchside to bedside to improve patient care utilizing advantages of the PAI system.

The desirable features of Clinical PAI systems are deeper imaging depth, wider field of view (FOV), and faster scan time than the laboratory-level PAI systems. The main components of PAI systems such as lasers, imaging probes, and data acquisition/processing systems are all being designed to meet these requirements. For deeper penetration, near-infrared pulsed lasers with the wavelength from 650 to 1100 nm are commonly used since they can maximize SNR in deep tissue with low extinction [40, 41]. High-power pulsed lasers are also used to obtain high SNR in deep and wide areas. However, the frame rate of the high-power pulsed lasers is low since the pulse repetition frequencies (PRFs) of these lasers are usually several tens of Hz. In addition, high-powered lasers are very expensive and bulky. Thus, low power, less expensive compact laser diodes and light emitting diodes (LEDs) are also used as an excitation source for PAI. These have weaker peak power but supports high PRF of several kHz. Thus, the signal can be acquired multiple times and averaged to improve the SNR [31, 42]. For larger FOV, clinical PAI systems utilize array transducers with multi-channel data acquisition systems. The linear array transducer of US imaging is the most standard form of the PAI probes used. Curved linear array transducers, convex or concave, are also used if a wider field-of-view than the one available using linear transducer is needed [38]. Between convex and concave, concave array transducers are more frequently used in PAI since they improve the SNR of the PA image and also the visibility of large-size vessels by mitigating the limited-view effect of the linear array transducers [43]. Moreover, volumetric array transducers are used in PAI for acquiring three-dimensional (3D) and four-dimensional data, i.e., real-time 3D, thanks to the advances in parallel processing and digital beamforming technologies [44]. Due to the inherent similarities with the existing US system, some commercially available US systems allow the user to modify the system for laser integration, PA beamforming and display to transform it into a clinical PAI system [45, 46]. Customized multi-channel data acquisition systems are used for acquiring PA signals from multiple transducers [29, 47–49]. In some applications that require a large tomographic view, motorized stages are used to control the position of PAI transducers synchronized with the data acquisition sequence [30, 49–51].

In this review, we summarize state-of-the-art clinical PAI systems along with three types of the imaging transducers: linear array transducer, curved linear array transducer, and volumetric array transducer. We will also discuss the limitations of the current PAI systems and describe latest techniques being developed to address these for further enhancing the image quality of PAI for successful clinical translation.

2 Clinical PAI platforms

2.1 Clinical PAI systems based on linear array transducers

In a clinical ultrasound imaging practice, high-frequency linear array transducer is commonly used to image small parts and shallow structures such as thyroid, breast, and blood vessel [52]. Not only because of its general use in clinical practice but also because of its suitability for conventional ultrasound and photoacoustic dual-modal imaging, linear array transducer is also the most commonly used transducer for clinical PA platforms, and the first CE-approved PAI product supports linear array transducer (Imagio, Seno Medical Instruments Inc., San Antonio, TX, USA). In this section, we will present a review of several PA imaging platforms with linear array transducer for various clinical applications such as breast cancer [53, 54], thyroid cancer [46, 55], vascular examination [30, 56], and inflammation [31, 32].

Many research groups are working on clinical PA imaging systems to image intrinsic optical contrasts (e.g., oxy-hemoglobin, deoxy-hemoglobin, melanin, lipid, water, etc.) and functional information (i.e., total hemoglobin concentration and hemoglobin oxygen saturation) of the cancerous tumor [4, 25, 46, 53–55, 57]. Summary of several clinical PA imaging platforms using linear array transducer is shown in Fig. 1. A handheld US imaging transducer combined with a laser delivery module, usually angled optical fiber bundle, is widely used in these PAI systems.

Recently, Neuschler et al. presented a pivotal clinical study of PA imaging to diagnose benign and malignant breast masses [54]. In this study, they categorized 2105 subjects with Breast Imaging Reporting and Data System (BI-RADS) scoring using PA/US images and standalone US images independently. The study used Seno Medical Instruments (San Antonio, TX, USA), which functions both as a stand-alone US imaging system and also as a dual-modal PA/US imaging system (Fig. 1a(i)). A single handheld probe consisting of a 128-element linear array transducer and a fiber optic bundle was utilized for duplex imaging [57, 58]. Functional color-coded PA data representing relative hemoglobin oxygenation and total hemoglobin concentration were obtained using a 757 nm Alexandrite laser and a 1064 nm Nd:YAG laser (Fig. 1-a(ii)). The optical penetration depth for PA imaging was
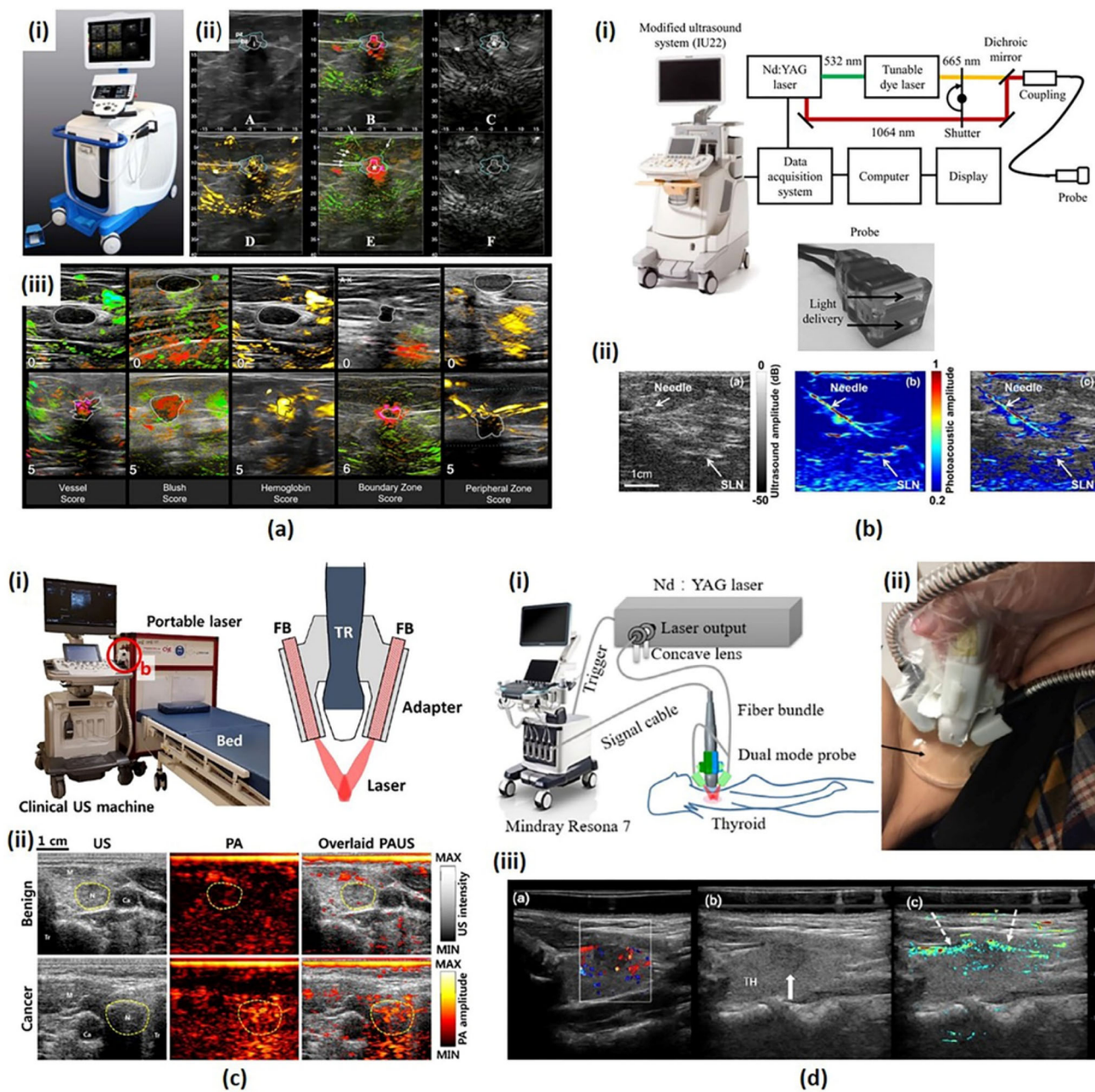
Fig. 1 a A duplex PA/US imaging system for in vivo breast cancer imaging. (i) A photograph of the system. (ii) A standard 6-on-1 PA image from a patient with invasive mixed ductal and lobular carcinoma. (iii) Exemplary images of minimum and maximum scores for five PA features. **b** A dual-modality PA/US imaging system for noninvasive SLN detection in breast cancer patients. (i) A schematic of the system. (ii) US, PA and co-registered US/PA images of SLN and needle. **c** A clinical PA/US imaging system for thyroid cancer imaging. (i) Photography of the system and a schematic of an integrated PA/US imaging probe. (ii) US, PA and overlaid PA/US images of benign and cancer cases. **d** A PA/US dual imaging system for human thyroid cancers. (i) A schematic of the system. (ii) A photograph of a dual-modality handheld probe. (iii) Color Doppler, US, and PA/US imaging results for a left lobe papillary thyroid cancer. All images were reproduced with permission from Refs. [46, 53–55]. *PA* photoacoustic; *US* ultrasound; and *SLN* sentinel lymph node

about 3 cm in the breast tissue. To compare the diagnostic sensitivity and specificity of PA/US versus US alone, seven breast imagers scored five PA features (Fig. 1a(iii)) and made BI-RADS assessment. The study results showed that PA/US images could increase the diagnostic specificity (43.0% for PA/US versus 28.1% for US alone) of breast masses without degrading the sensitivity (96.0% for PA/US versus 98.6% for US alone).

Garcia-Uribe et al. developed a dual-modal PA/US imaging platform for noninvasive sentinel lymph node

(SLN) detection in breast cancer patients [53]. The study was performed using a modified clinical US system (iU22, Philips Healthcare), linear array transducers (L12-5 and L8-4, Philips Healthcare), and a tunable dye laser (PrecisionScan-P, Sirah, Kaarst, Germany) pumped by an Nd:YAG laser (QuantaRay PRO-350-10, Spectra-Physics, Santa Clara, CA). They used a bifurcated fiber bundle that flanked the linear array transducer for delivering 667 nm laser with a pulse duration of 6.5 ns and a repetition rate of 10 Hz. A custom-built data acquisition (DAQ) system was used to transfer per-channel data from the transducer to a computer. The computer was then used to reconstruct PA, US, and co-registered PA/US images, and display the images (Fig. 1b(i)) at 5 frames per second. They proposed a minimally invasive PA/US image-guided fine needle aspiration biopsy (FNAB) of a sentinel lymph node (SLN) for the staging of breast cancer. They enrolled sixteen women for their clinical study and they successfully guided FNAB for axillary staging. The SLN and the needle images using this PA system were clearly visualized with high contrast than the conventional US image (Fig. 1b(ii)).

Using a recently developed PA/US imaging platform [45], Kim et al. conducted a pilot clinical study to distinguish malignant and benign thyroid nodules [55]. They used an FDA-approved programmable US system (EC-12R, Alpinion Medical Systems) and a portable laser system (Phocus, Opotek Inc.) consisting of a pulsed Nd:YAG pump laser and an optical parametric oscillator (OPO), which tunes the wavelength in the range of 680–950 nm. A bifurcated optical fiber bundle was used for laser delivery mounted on a 128-element linear array transducer (L3-12, Alpinion Medical Systems) using a custom-designed adapter (Fig. 1c(i)). They aligned the two fiber bundles so that the laser power converges to a depth of 2 cm from the surface of the transducer, which is the typical depth of the thyroid from the skin surface. At each trigger signal, generated at Q-switch firing, the PA signals were received and

digitized using a 12-bit 64-channel DAQ present inside the Alpinion US machine. They used 760, 850, 930, and 950 nm excitation wavelengths to represent deoxygenated hemoglobin, oxygenated hemoglobin, lipid, and water, respectively. The output energies of each wavelength were 11.0, 10.7, 10.3, and 9.8 mJ/cm^2, respectively. The PA signals from 34 patients were analyzed, and the PA signals from the malignant nodules were found to be higher than those from the benign nodules (Fig. 1c(ii)).

Another clinical study of thyroid cancers was performed by Yang et al., which uses a PA/US handheld probe [46]. A dual-modal PA/US system was developed based on a clinical US machine (Resona7, Shenzhen Mindray Bio-Medical Electronics Co., Ltd.) and a 1064-nm Q-switched Nd:YAG laser (LS-2137/2, LOTIS TII). A 192 elements 5.8 MHz linear array transducer (L9-3U, Shenzhen Mindray Bio-Medical Electronics Co., Ltd.) and a bifurcated optical fiber bundle were integrated into a handheld duplex imaging probe (Fig. 1d(i)). The surface of the transducer was covered with a thin film made of silica gel and TiO$_2$ particles to eliminate artifacts caused by the laser irradiated on the surface of the transducer. A 7 mm thick transparent gel pad was placed between the imaging site and the probe to gather the two laser outputs onto the imaging plane (Fig. 1d(ii)). Five PA images were averaged to improve SNR and the total acquisition time for dual-modal PA/US imaging was one second. Grayscale US images, color Doppler flow images (CDFI), and PA/US dual images were acquired for all 13 subjects, 10 patients with cancerous thyroid nodule and 3 healthy volunteers. The study results revealed higher imaging sensitivity in PA images for peripheral and intra-nodular blood vessels than the CDFI (Fig. 1d(iii)).

Figure 2 summarizes linear array based clinical PA platforms for vessel visualization. Current vascular imaging modalities in clinical practice including CT angiography, MR angiography, and US Doppler imaging, have
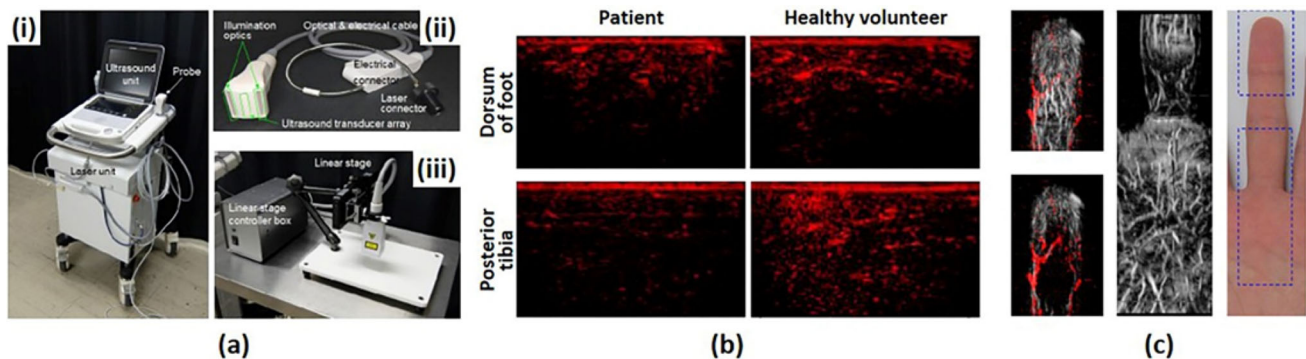

Fig. 2 a A PA/US imaging system for peripheral small-vessel imaging. (i) A photograph of the system. (ii) A photograph of a handheld type PA probe. (iii) A photography of a linear stage scanner for 3D image acquisition. b PA images of a diabetic foot patient and a healthy volunteer. c Overlaid PA–US Doppler and PA MAP images and a photograph of a human finger. All images were reproduced with permission from Ref. [30]. PA photoacoustic, US ultrasound, MAP maximum amplitude projection

limitations such as use of contrast agent, exposure to ionizing radiation, poor usability, low resolution, or combinations of the above. Since PAI can show high-contrast and high-resolution vascular images without exogenous contrast agent or ionizing radiation, it provides complementary information about the blood vessel especially peripheral small vessel, which is difficult to visualize using conventional modalities.

Irisawa et al. presented a clinical PA imaging platform for small vascular imaging and performed an early feasibility study for diabetic foot patients [30]. They used a previously developed PA imaging system [59] consisting of a commercial portable US system (FUJIFILM FC1, FUJIFILM Medical Co., Ltd.) and a lightweight Alexandrite laser unit for a compact design suitable for clinical environments (Fig. 2a(i)). The laser fired 750 nm pulses and these pulses were delivered to illumination optics through optical fiber bundles attached to both sides of a linear array transducer (Fig. 2a(ii)). The optical fluence at the optics was 14.3 mJ/cm^2, which is well below the ANSI safety limit. They used the white-colored acoustic lens on the transducer to reflect the incoming light to the transducer surface. This lens reduced the interfering signals and also increased the efficiency of laser delivery. To test the feasibility of the system, they obtained PA images of a diabetic foot patient and a healthy volunteer, showing lower signal level and poor signal distribution in the patient compared to the normal subject (Fig. 2b). They also

obtained 3D images of human finger and palm using a linear scanning stage and a machine arm as shown in Fig. 2a(iii). They successfully visualized small vessels with low flow velocity using 3D PA imaging which provides complementary information to US Doppler imaging (Fig. 2c).

A linear array transducer is also used in designing a clinical photoacoustic computed tomography system for evaluating the mechanical properties of biological tissues [56, 60]. A vascular elastic photoacoustic tomography (VE-PAT) system proposed by Hai et al. [51] for vascular compliance measurements in humans is shown in Fig. 3a. The imaging system consists of a 256-element linear array US transducer with a central frequency of 21 MHz (LZ250, Visualsonics Inc.) and two optical fiber bundles mounted on each side of the transducer (Fig. 3a). The two fiber bundles were tilted at an angle of 30 degrees to the imaging plane so that the light converges at 15 mm depth from the transducer surface, which is the elevation focal length of the transducer. The excitation wavelength was set to 850 nm using a tunable OPO laser for deep penetration depth. The optical fluence on skin was 10 mJ/cm^2, which is well below the safety limit. PA images were acquired by a commercial PA imaging system (Vevo LAZR, Visualsonics Inc.) before and after applying an external compression force on samples using a customized compression stage (Fig. 3b). Experimental results confirmed that the VE-PAT successfully assessed reduced vessel compliance in a
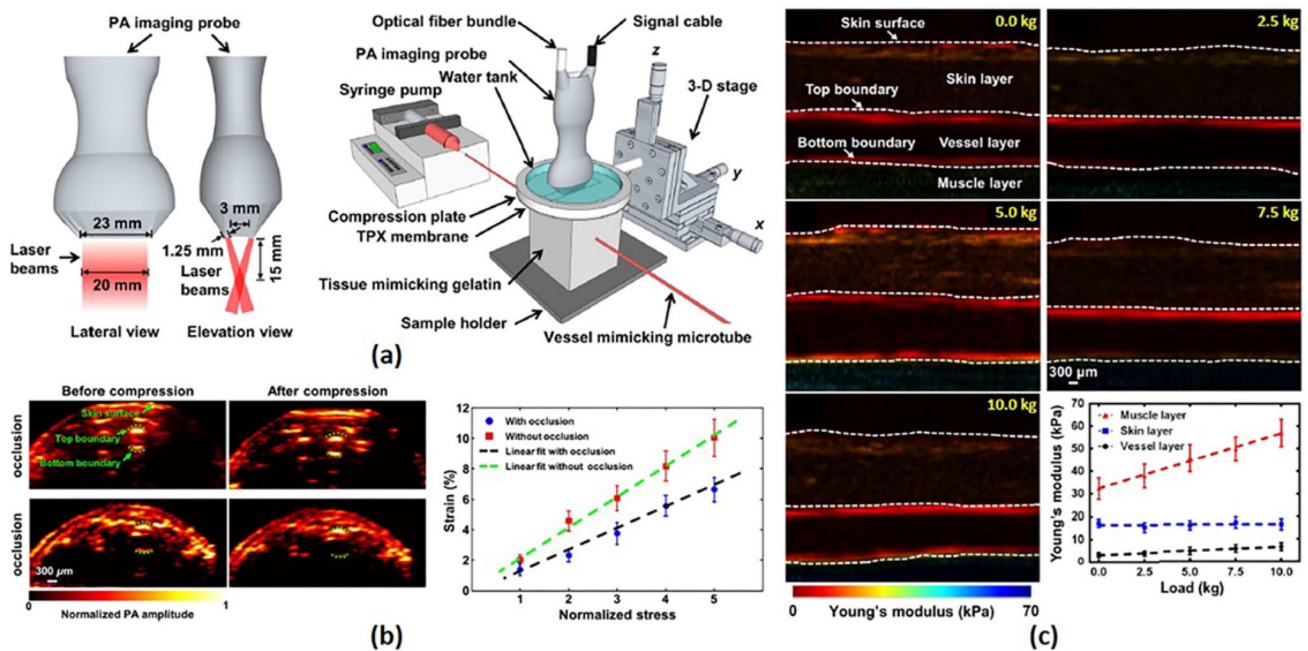

Fig. 3 **a** A schematic of VE-PAT. **b** VE-PAT images of a human finger without vessel occlusion before and after compression and with vessel occlusion before and after compression and corresponding strain–stress curve. **c** QPAE of the human arm at different loadings. All images were reproduced with permission from Refs. [56, 60]. *VE-PAT* vascular elastic photoacoustic tomography, *QPAE* quantitative photoacoustic elastography

human finger with occluded vessel (Fig. 3c). Further, they extended their work for quantitative PA elastography (QPAE) to assess absolute elasticity of biological tissue in humans [60]. Using silicone rubber with the known stress–strain property, the QPAE mapped the absolute Young's modulus up to 6 mm depth in the human arm (Fig. 3d).

PA/US dual imaging systems using linear array transducer for arthritis patients are summarized in Fig. 4. PA images of human fingers were obtained with integrated PA/US probes to evaluate hyper-vascularity and hypoxia, which are early findings of inflammation.

Van den Berg et al. reported a dual modality PA/US system with a handheld probe for synovitis assessment in rheumatoid arthritis patients [31]. As shown in Fig. 4a(i), the probe fully integrated a US transducer and a compact diode laser module in a size comparable with a US imaging probe used in the current clinical practice [61]. They used a commercial 128-element linear array transducer (SL3323, ESAOTE) with a central frequency of 7.5 MHz and connected it to a modified portable US system (MylabOne, ESAOTE). The cost-effective diode laser source (Quantel Laser) was driven by a customized laser driver (Brightloop) and emitted 1 mJ pulses with a wavelength of 808 nm, the isosbestic point of oxygenated and deoxygenated hemoglobin. This selected wavelength acquires PA signals independent of hemoglobin oxygenation. Unlike most linear array-based systems using optical fiber bundles for laser delivery, they inserted the compact laser module into the imaging probe and irradiated the light onto the imaging plane using cylindrical micro-lenses and diffusive optical elements. To prevent the probe from overheating, an aluminum rim was attached to the probe to increase the air cooling efficiency. US Doppler and PA/US scans were performed with the patient's hand submerged in water and rested on supports (Fig. 4a(ii)). As shown in Fig. 4a(iii), the system visualized inflamed joints with distinguishable PA amplitude from non-inflamed joints, which demonstrates the ability of the system in detecting synovitis.

A similar clinical study for identifying inflammatory arthritis in human joints was reported by Jo et al. [32]. Focusing on the capability of PA imaging for evaluating hemodynamic changes, metacarpophalangeal (MCP) joints were imaged with a PA/US dual imaging system using two excitation wavelengths, 576 and 584 nm for oxy- and deoxy-hemoglobin, respectively. A commercial research US platform (V1, Verasonics) and a tunable dye laser (ND6000, Continuum) pumped by the second harmonic of an Nd:YAG laser (Powerlite, Continuum) were integrated to build the PAI system [62, 63]. A custom-design probe holder integrated a linear array transducer (CL15-7,
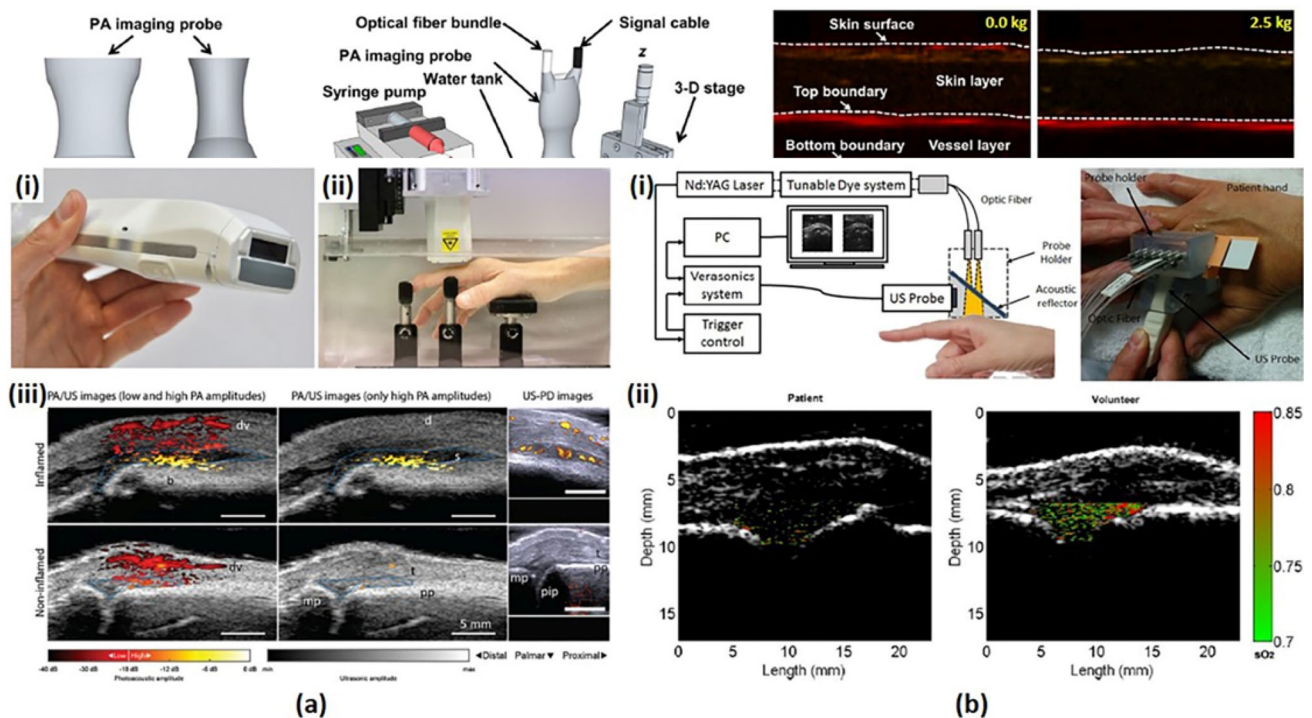

Fig. 4 a A dual modality PA/US system for synovitis imaging. (i) A photograph of a handheld PA/US probe. (ii) A sample positioner for human finger imaging. (iii) PA/US and US Doppler images of inflamed and non-inflamed contra-lateral joint. b A PA/US dual imaging system for inflammatory arthritis in the human joint. (i) A schematic and a photograph of the system. (ii) PA sO_2 images of a patient's MCP joint and a healthy volunteer's MCP joint. All images were reproduced with permission from Refs. [31, 32]. *PA* photoacoustic, *US* ultrasound, sO_2 oxygen saturation, *MCP* metacarpophalangeal

Philips) and an optical fiber bundle (CeramOptec Industries Inc.) into one body as shown in Fig. 4b(i). An optically transparent acoustic reflector was placed inside the holder to transmit the light irradiated from the optical fiber to the imaging region and to reflect the generated PA signals back to the ultrasound transducer. All spaces in the probe holder were filled with US coupling gel. Figure 4b(ii) shows PA oxygen saturation (sO$_2$) image of arthritis patient's joint and heathy volunteer's joint, demonstrating decreased hemoglobin oxygenation in patients with inflamed synovitis compared to the normal subjects.

2.2 Clinical PAI systems based on curved linear array transducers

In general, curved linear array transducers are available in two forms: convex and concave. The convex array transducer, also known as curved linear array transducer, is typically used in the ultrasound applications which requires large FOV and deep imaging depth, e.g., OB/GYN and abdominal studies. Also, convex array transducer is miniaturized for specialized endocavity ultrasound applications, such as urology and cardiac applications. Concave array transducer is not used for US imaging but is promising for PA imaging applications. Since PA wavefronts propagate almost isotropically from the signal sources, wide-angle concave array has the optimal arrangement of the transducer elements for fully utilizing their receiving directivity resulting in high SNR. In this section, we summarize clinical PA imaging platforms that use concave and convex array transducers for various clinical studies, e.g., thyroid [47, 64], breast [48], peripheral vasculature [29, 49, 50], prostate [38] and uterine studies [65].

Curved linear array transducers are used in the studies based on Multi-Spectral Optoacoustic Tomography (MSOT) platforms [29, 47, 48, 64]. Commonly, they fabricate real-time handheld probes by integrating fiber bundles inside the transducers. Water is filled inside the center cavity of the concave arc and is sealed with transparent membranes for gel-coupling with the skin. Because of the cavity in the center, light can be delivered directly to the imaging plane thus optimizing light fluence inside the FOV and minimizing out-of-plane artifacts [29]. For multispectral analysis of the tissue components, they use tunable OPO lasers that can quickly tune the wavelength for each consecutive pulse. For fast pulse-by-pulse data acquisition and image reconstruction, they used customized data acquisition systems with a large number of receiving channels (more than or equal to the number of transducer elements) and graphics processing units (GPUs) for accelerated image processing. The water inside the cavity

can be replaced with heavy water that has lower optical absorption in NIR regions.

Dima et al. developed an MSOT platform with a concave array transducer to image human carotid in vivo [47]. The concave array was half-arc (172° spanning range, 80 mm diameter, 64 elements, 5 MHz center frequency) with an ROI of 20 mm × 20 mm (Fig. 5a(i and ii)), and spatial resolutions of 1 mm (elevation) and 150 μm (cross-sectional). They used an Nd:YAG-pumped tunable OPO laser (50–90 mJ/pulse, 690–900 nm, 5 ns pulse length, 10 Hz PRF, Opotek Inc.) and delivered it with a fiber bundle resulting in an average fluence of 13 mJ/cm^2 (< 32 mJ/cm^2 @ 800 nm, ANSI maximum permissible exposure level). They used a custom-made 128-channel DAQ with a sampling rate of 40 MSamples/s. The digitized signals were averaged ten times to improve the SNR. Through phantom experiments, they showed the superiority of the concave array transducer over a linear array transducer (Acuson L7, 128 elements, 5–7 MHz, Siemens Healthcare) regarding SNR and ability of the system to reconstruct circular structures without distortion. To test the system feasibility in vivo, they successfully acquired a PA image of the common carotid artery and the adjacent jugular veins (Fig. 5a(iii)). With the same transducer configuration and enhanced light delivery, they acquired in vivo PA images of healthy human thyroids. These images showed major structures around the thyroid and also better-resolved vasculature as shown in Fig. 5a(iv) [64].

Diot et al. conducted a pilot study to image breast cancer with a handheld real-time MSOT transducer [48, 66]. Similar to the previously discussed concave transducers, this probe was comprised of a half-arc array transducer (174° spanning range, 120 mm diameter, 256 elements, 5 MHz center frequency), with an Nd:YAG-pumped tunable OPO laser (15 mJ/pulse (max.), 680–980 nm, 8 ns pulse length, 50 Hz PRF; InnoLas Laser) delivered by a custom-made fiber bundle. For dry-type acoustic coupling, the cavity inside the arc was filled with heavy water and sealed with low-density polyethylene membrane. Detected signals were digitized by a custom-made 12-bit 256-channel DAQ with a sampling rate of 40 MSamples/s. The acquired data for each laser pulse was reconstructed to form a PA image using model-based algorithm [67] and accelerated with the GPU for real-time display. For multispectral analysis of the breast tissue, 28 PA frames were acquired by varying wavelength from 700 to 970 nm with 10 nm incremental steps and were decomposed into four component distribution maps (Hb, HbO$_2$, lipid, water) via spectral unmixing [68]. Using this system, they could differentiate the distribution of four components in the normal and cancerous breasts, especially the neovascularization patterns around the tumor region.
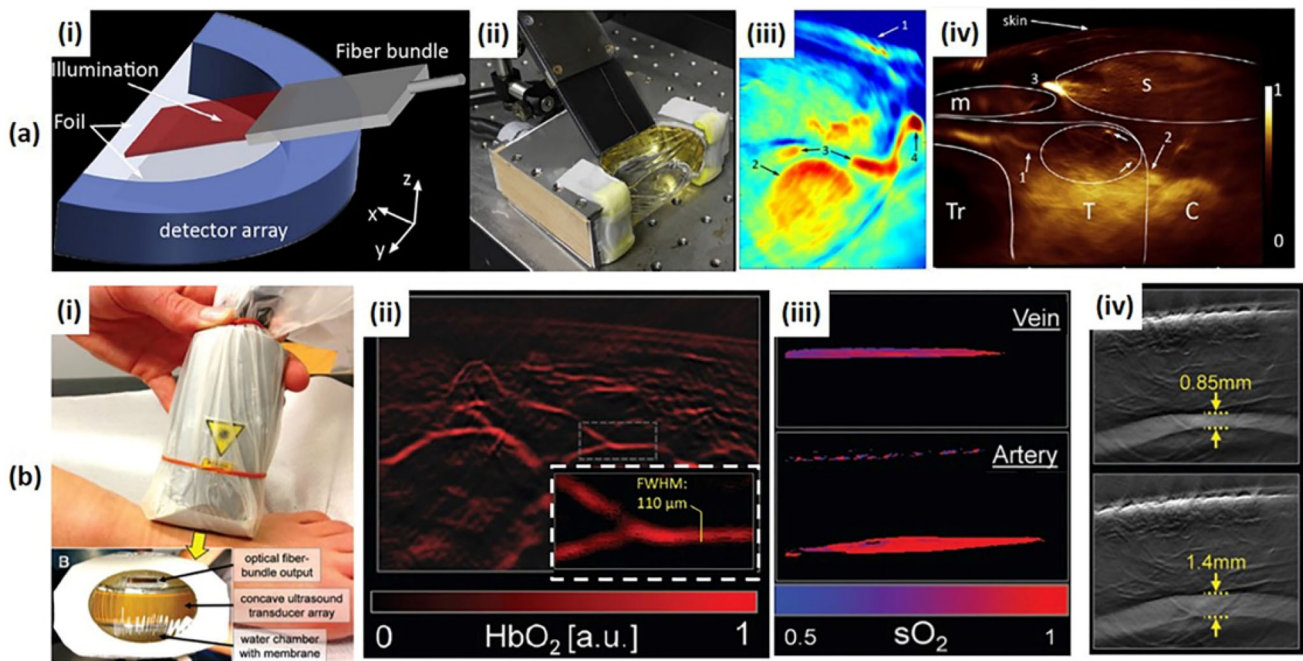
Fig. 5 a An MSOT system for in vivo human neck imaging. (i) A schematic and (ii) a photograph of an MSOT imaging probe for human carotid and thyroid. (iii) An MSOT image of human carotid artery. 1: Skin surface; 2: Common carotid artery; 3: Internal jugular vein; 4: External jugular vein. (iv) An MSOT image of a healthy human thyroid. T: Thyroid; C: Carotid artery; Tr: Trachea; s: sternocleidomastoid muscle; m: infrahyoid muscle. **b** An MSOT system for in vivo human peripheral vasculature imaging. (i) A photograph of an MSOT imaging probe for human peripheral vasculature. (ii) An MSOT image of microvasculature in a human foot. (iii) An MSOT image showing the oxygen saturation of vein and artery. (iv) An MSOT image showing the pulsatility of tibialis posterior artery. All images were reproduced with permission from Refs. [29, 47, 64]. *MSOT* Multi-spectral optoacoustic tomography; sO_2 oxygen saturation

Taruttis et al. investigated the feasibility of a handheld MSOT scanner for assessing the vasculature of extremities [29]. They used MSOT system (EIP-100; iThera Medical) with a concave array transducer (135° spanning range, 128 elements, 8 MHz center frequency, 2 cm focal length) and an Nd:YAG-pumped tunable OPO laser (InnoLas Laser) delivered by an integrated fiber bundle (Fig. 5b(i)). The PRF of the laser was lowered from 50 to 10 Hz for delivering higher laser energy, and specific wavelengths of 730, 750, 800, and 830 nm were selected for obtaining blood composition (Hb, HbO_2) information. Generated data was acquired by a custom-made 12-bit digitizer with a sampling rate of 40 MSamples/sec, and were reconstructed to form a PA image using a model-based algorithm [67] built using OpenCL language. The system could provide high-resolution images of the blood vessels in the foot down to 90 μm (FWHM), which could not be visualized from US color Doppler images (Fig. 5b(ii)). The blood vessels can be classified into arteries and veins using oxygen saturation mapping provided via spectral unmixing [69] (Fig. 5b(iii)). The pulsation of the posterior tibialis artery can also be visualized (Fig. 5b(iv)).

Concave array transducers are also used in tomographic scanners for imaging human extremities [49, 50].

Commonly, they used motorized stages (either rotational or translational) to collect cross-sectional images from different positions and are then processed to form a 3D volume of the scanned targets, e.g., human finger. The 3D rendered tomographic images of the fingers showed microvasculature of the finger in a 360° view, which provides diagnostic information of microcirculation or neovascularization in the fingers.

Ermilov et al. developed an optoacoustic microangiography system (OmAS) for imaging blood vessels in human finger [50]. The system structure was derived from a 3D photoacoustic tomography system for small animals [70]. The probe of the system consisted of concave array transducer (152° spanning range, 130 mm diameter, 128 elements, 5 MHz center frequency), and an alexandrite laser (100 mJ/pulse, 755 nm, 75 ns pulse length, 10 Hz PRF; Light Age, Inc.) delivered by a bifurcated and randomized fiber bundle. The array transducer and the fiber bundle were integrated in a bowl-shaped chamber filled with vegetable oil that acts as an acoustic coupling medium and reduces the noise coming to the transducer. A rotational stage was used to rotate the probe around the finger dipped inside the bowl to produce 3D PA tomographic images (Fig. 6(i)). A 2D PA slice at each angular step was
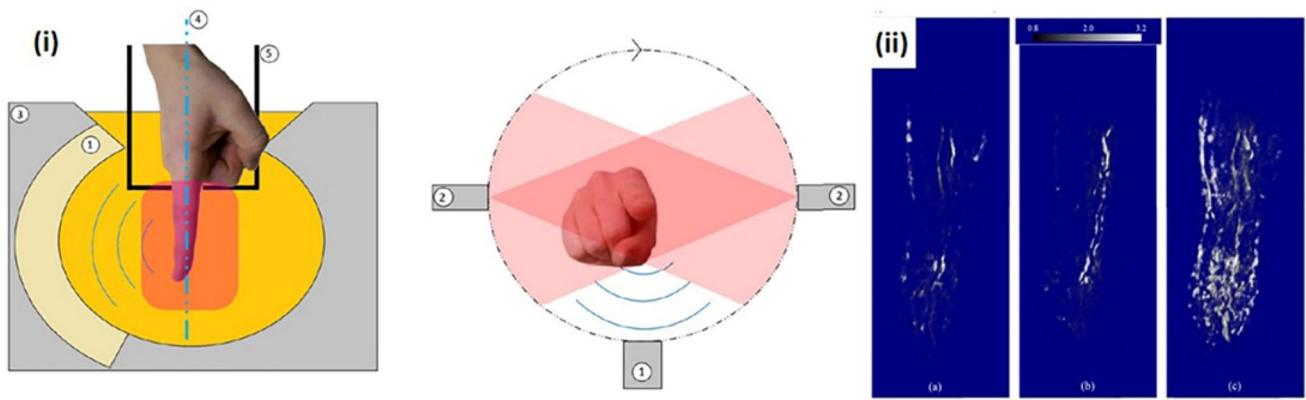
Fig. 6 An optoacoustic microangiography system (OmAS) for in vivo human finger imaging. (i) A schematic of the OmAS. (ii) Reconstructed 3D microangiograph of an index finger of a healthy volunteer at 1, 3, and 7 min after hypothermia stress test. All images were reproduced with permission from Ref. [50]

made from single laser pulse excitation and was captured with a sampling frequency of 20 MHz with a 60 dB amplification. The total scan time for 360° data acquisition was less than 30 s. As shown in Fig. 6(ii), the system could visualize the vasculature of the finger in 3D, which showed the potential of using this system for monitoring blood circulation problems in the fingers.

Oeri et al. reported a hybrid PA/US tomography system for finger imaging, mainly for diagnosing rheumatoid arthritis [49]. While most of the related systems are pre-clinical or experimental, this system is a dedicated diagnostic platform designed for finger joint imaging. The system used four arc-shaped capacitive micromachined ultrasound transducer (CMUT) arrays forming a ring shape. Advantages of CMUTs for designing concave PA signal detector are many including wide detection bandwidth, high directivity, and good manufacturing process. Each of the two larger arcs contained eight 32-element linear CMUT arrays resulting in 256 elements and each of the other two smaller arcs contained four 32-element linear CMUT arrays resulting in 128 elements (768 elements in total). Excitation frequency for US transmission mode was 10 MHz, and the center frequencies for PA reception were 11 MHz (smaller arcs) and 14 MHz (larger arcs, 15-MHz bandwidth), respectively. Each arc contained six laser beam outputs that delivered the laser from an Nd:YAG-pumped tunable OPO laser (680–980 nm wavelength, 6 ns pulse length, 100 Hz PRF; Ekspla) resulting in the fluence of 2.9 mJ/cm^2. Detected signals were acquired by a custom-made programmable platform supporting up to 1024 receive channels. The motorized scanning system controls all four arcs at once (for distal and peripheral interphalangeal joints) or two at a time (for metacarpophalangeal joint). The FWHM resolutions of the system are 160 μm for the US and 150 μm for PA imaging. They tested the feasibility of the system using a 3D PA/US tomography image finger phantom made of polyvinyl alcohol with chicken bones and black nylon sutures. They also performed an in vivo test with a volunteer finger and showed that the system could provide PA microvasculature images overlaid onto the anatomical US images.
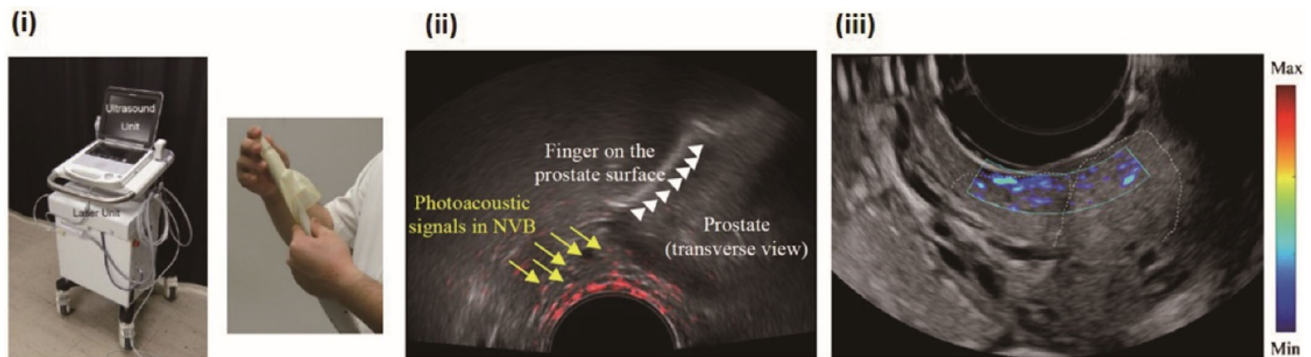

Fig. 7 A PA/US endocavity imaging system. (i) A photograph of the PA/US endocavity imaging system and the imaging probe. (ii) Overlaid PA/US image of a patient with prostate cancer. (iii) Overlaid PA/US image of a patient with uterine cervical cancer. All images were reproduced with permission from Refs. [38, 65]. *PA* photoacoustic, *US* ultrasound

Convex array transducers in a miniaturized form are used clinically in PA/US endocavity imaging [38, 65]. In contrast to concave array transducers, the convex array transducer elements are aligned divergently, thus enabling a large FOV. Endocavity ultrasonography has been used in transrectal imaging for prostate cancer and transvaginal imaging for uterine/endometrial/cervical cancer. The angiogenesis seen in a US Doppler imaging has been conventionally used as an indicator for suspicious cancer. The PA imaging system, which visualizes microvasculature at a higher resolution than conventional Doppler would provide added advantage to diagnose pathologies. The PA/US endocavity imaging system, shown in Fig. 7(i), consists of a portable US system and a laser source. A microconvex array transducer (170° spanning range, 6.5 MHz center frequency) was combined with the fiber bundles, and they delivered output from an alexandrite laser (755 nm wavelength, 40–50 ns pulse length, 10 Hz PRF) with a spanning range of 160° to give an average fluence of 15 mJ/cm^2. The in vivo imaging results of a prostate cancer patient and a uterine cervical cancer patient showed increased PA signals near the tumor lesion indicating the signs of angiogenesis (Fig. 7ii, iii).

2.3 Clinical PAI systems based on volumetric array transducers

A volumetric array transducer basically consists of a 2D or 3D alignment of transducer elements for acquiring 3D volumetric data of the imaging target. The volumetric array transducer can acquire a 3D volume at a single position or can be mounted on a motorized scanning stage for an extended FOV. Because of the wide detection angle, especially for a hemispherical array, the volumetric transducer is very suitable for PA signal reception. The volumetric array transducer system requires a data acquisition system capable of acquiring a large number of channels

and also a processing unit with high computational power to process the 3D data. In this section, we summarize 3D PA imaging platforms that use a 2D circular array transducer [71–73] and a hemispherical array transducer [44, 51, 74, 75].

The Twente Photoacoustic Mammoscope [72, 73] used a circular 2D array transducer, which was originally developed for an ultrasonic bone densitometer (Achilles Insight^{TM}). The transducer was made with a single 90 mm diameter circular polyvinylidene fluoride (PVDF) sheet activated by 588 gold electrodes arranged on this PVDF sheet. This results in a volumetric transducer with 588 independent PVDF elements with a center frequency of 1 MHz and a bandwidth of 130%. The system used a Q-switched Nd:YAG laser (1064 nm wavelength, 10 ns pulse length, 10 Hz PRF; Quantel) coupled to a custom-made light delivery system comprised of prisms. A scanning system moved the light delivery system in two axes to illuminate the whole breast area. In the first prototype system [72], data were acquired using only one channel of a dual-channel 8-bit 100 MSamples/sec digitizer card (NI-5112, National Instruments), which took about 25 min to scan a FOV of 45 × 45 mm. In an upgraded version of the system, signals from all 588 elements were grouped into 10 sectors, were buffered and amplified with 10 Application Specific ICs (ASICs) and acquired in parallel using two 8-channel 12-bit 60 MSamples/s digitizers (NI PXI 5105, National Instruments). This system accelerated the scanning time and took less than 10 min for a FOV of 90 × 85 mm. For an infiltrating ductal carcinomas (IDCs), the system provided PA signal patterns well matched to the corresponding MR images and the histopathologic results.

Toi et al. reported photoacoustic mammography results using the PAM-03 system developed by Canon Inc. in collaboration with Optosonics [51, 74]. The system was developed based on a 127 mm diameter hemispherical array transducer embedded with 512 elements having
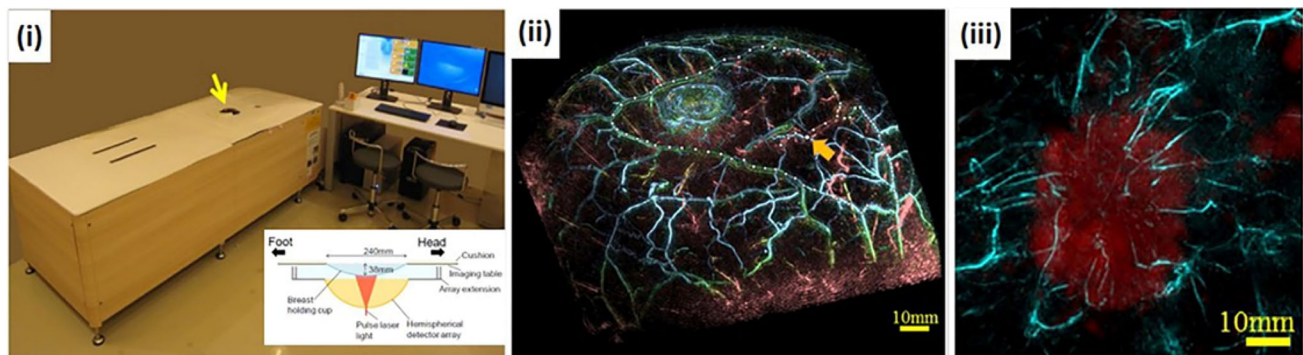

Fig. 8 The PAM-03 PA mammography system. (i) A photograph and a schematic of PAM-03. (ii) A PA mammography image of a normal breast where the colormap indicates the depth. (iii) An overlaid PA (cyan)/MR (red) image of a tumor lesion. All images were reproduced with permission from Ref. [51]. *PA* photoacoustic, *MR* magnetic resonance. (Color figure online)

2 MHz center frequency and 70% bandwidth. The center of the hemisphere was punctured to deliver the light output from a Q-switched dual-wavelength alexandrite laser (200 mJ/pulse, 755 and 795 nm wavelength, 75 ns pulse length) with a 60 mm diameter illumination area. The cavity in the center of the hemisphere was filled with reverse osmosis water for acoustic coupling and covered by a breast cup made of transparent polyethylene terephthalate (Fig. 8i). The transducer was mounted on a 2D motorized stage to move the scanner in a spiral pattern for a larger FOV. The central region of the breast was more densely scanned to enhance the signal from the deepest part of the breast. The imaging area was selectable from 50, 70, and 100 mm radius and the number of acquisitions per scan is also selectable from 1024 and 2048, which corresponds to the scan time of 51.2 and 102.4 s, respectively. The total scan time using two wavelengths and 2048 acquisitions were about 4 min. The PAM-03 system could visualize fine vasculature of the breast (Fig. 8ii), and showed indications of abnormal blood vessel formations near the tumor when compared with overlaid MR images (Fig. 8iii).

While the above systems provided tomographic images of the large FOV, Deán-Ben and Razansky developed a real-time handheld volumetric MSOT (vMSOT) for functional real-time PA images of relatively small FOV [44]. The transducer consisted of 256 piezocomposite elements (3 × 3 mm, 4 MHz center frequency, 100% bandwidth) arranged in a hemispherical pattern with 40 mm radius and 90° solid angle. The center of the hemisphere was punctured for fiber-guided light delivery of an Nd:YAG-pumped tunable OPO laser (690–900 nm wavelength, < 10 ns pulse length, 10 Hz PRF; Opotek Inc.). The cavity of the hemisphere was filled with water for acoustic coupling and sealed with transparent polyethylene membrane (Fig. 9i). Signals from all 256 independent

transducer elements were acquired in parallel by 16 data acquisition cards, each with 16 channels and 40 MSamples/s. The spatial resolutions of the system were 300–500 μm (axial) and 200–400 μm (lateral) in the central region of the hemisphere. The vMSOT system could visualize changes in the blood flow in real-time using a single 900 nm wavelength (Fig. 9ii) and could distinguish veins and arteries using multi-spectral imaging (Fig. 9iii). For a clinical application of vMSOT, Chual et al. [75] investigated its use on skin cancer patients providing the distribution of melanin as well as oxy-/deoxy-hemoglobin (Fig. 9iv).

3 Current issues and future outlooks

Since PAI is based on ultrasound detection, early PA studies were performed using conventional US systems. Using conventional US system is more advantageous since it facilitates easy clinical translation by providing PA images in addition to the US images. Linear arrays are used extensively in this respect, but PA images appear to be distorted due to the limited view effect of the linear probes [43]. Concave array transducer mitigates this problem by providing a wide angle, but can only image small regions located at the center of the arc. Deán-Ben et al. introduced a hybrid-array-based optoacoustic and US (OPUS) transducer to avoid the limited-view effect while maintaining large FOV for linear array transducers [76] (Fig. 10a). The hybrid array transducer has an intermediate linear array and the concave array at both ends of the array. They achieved a wide FOV of 40 mm × 40 mm and reconstructed US and PA image using the 128 elements of the linear array and all the 256 elements of the linear and concave array, respectively, while minimizing the limited-view effect.
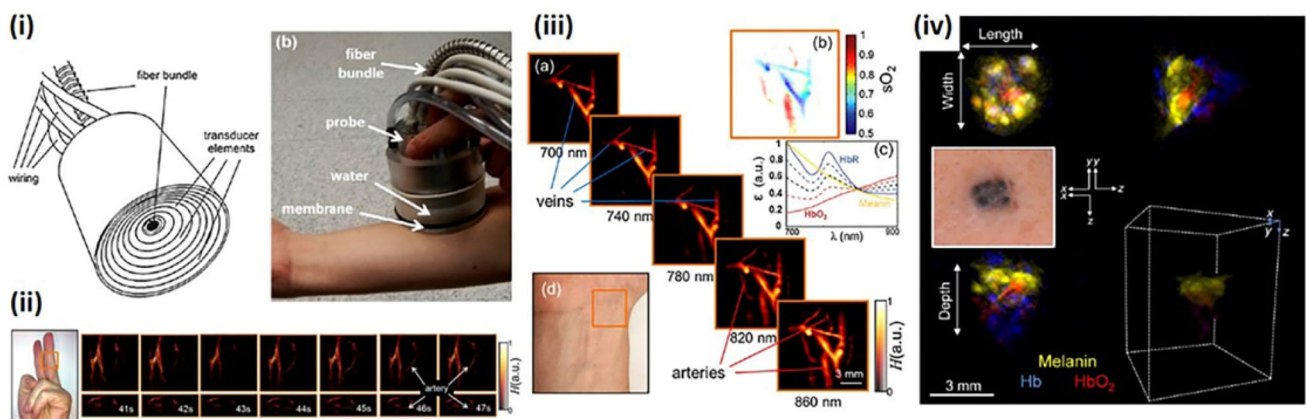
Fig. 9 A real-time vMSOT probe. (i) A schematic and a photograph of the real-time vMSOT probe. (ii) Real-time vMSOT images showing changes in the blood flow when the rubber band was released from the finger at 42 s. (iii) Multi-spectral vMSOT images showing veins and arteries of a human wrist. (iv) A photograph and multi-spectral vMSOT images of a patient with skin cancer. All images were reproduced with permission from Refs. [44, 75]. *vMSOT* volumetric multi-spectral optoacoustic tomography

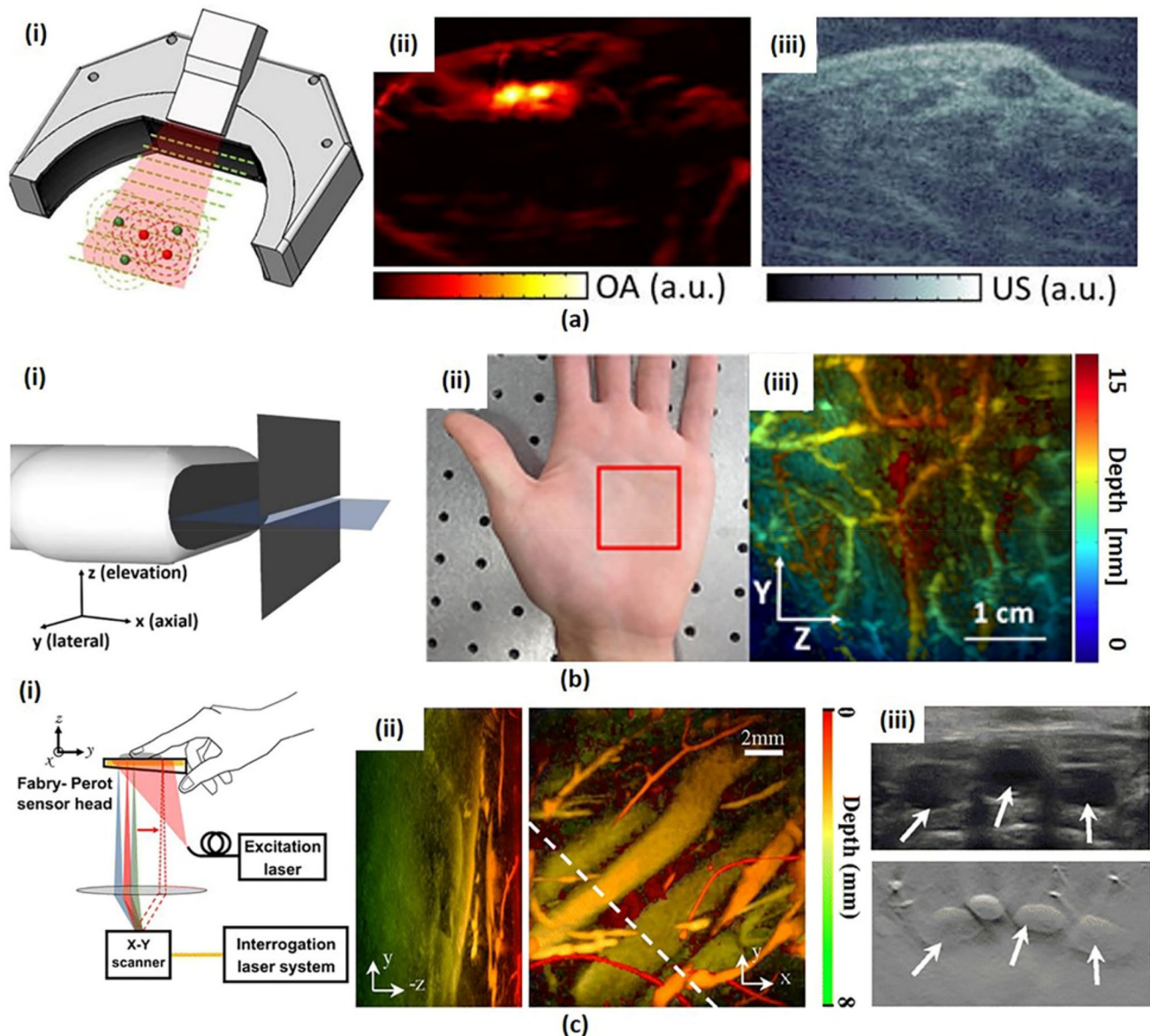**Fig. 10 a** Hybrid-array-based optoacoustic and US (OPUS) transducer. (i) Schematic. (ii) PA image of a human wrist and (iii) the corresponding US image with the same OPUS imaging probe. **(b)** Slit-based PA tomography system. (i) Schematic. (ii) Photograph of a human palm and (iii) depth-encoded vascular image (iii) of the indicated region with red box in (ii). **(c)** FP PA imaging system. (i) Schematic. (ii) Volumetric PA images of human dorsalis pedis projected in X-axis (left) and Z-axis direction (right). (iii) US image (top) and corresponding PA B-mode image (bottom) from the highlighted region in (ii) with a white dashed line. All images were reproduced with permission from Refs. [76, 79–81]. *PA* photoacoustic, *OPUS* optoacoustic-ultrasound, *FP* Fabry–Perot

Both the linear array and the curved array usually have a 1D array of elements providing cross-sectional 2D images. However, it is difficult to locate a lesion by relying solely on the cross-sectional image, and the clinical outcome depends on the skill of the user while using this 1D array transducer to identify the suspicious region correctly. A 2D array transducer may be an ideal solution to address this problem. However, to image the wide ROI without deteriorating image quality, it is necessary to increase the number of elements and channels in the limited size of the

2D array. Thus, as a simple and cost-effective alternative to the 2D array, several attempts have been made to scan the ROI with a mechanically translated 1D-array transducer. However, due to the relatively poor elevational resolution of the 1D-array transducer, a uni-directional scan cannot provide isotropic spatial resolution. To address this issue, Gateau et al. and Schwarz et al. proposed a rotational scanning method and a bi-directional scanning method, respectively [77, 78]. More recently, Wang et al. introduced a simpler and cost-effective method of placing a

Table 1 Specifications of clinical photoacoustic imaging platforms

Platform	Probe					Laser				Light delivery	Data acquisition/ processing system	Application
	Transducer type	# Of elements	Center frequency	Bandwidth	Scanning type	Wavelength	PRF	Pulse duration	Power			
Neuschler et al. [54]	Linear	128		4–16 MHz	Handheld B-scan	757, 1064 nm		< 100 ns		Fiber		Breast cancer
Garcia-Uribe et al. [53]	Linear	128		4–12 MHz	Handheld B-scan	667 nm	10 Hz	6.5 ns	< 10 mJ/cm²	Fiber	iU22 (Philips Healthcare)	Breast cancer
Kim et al. [55]	Linear	128	8.5 MHz	3–12 MHz	Handheld B-scan	760, 850, 930, 950 nm	10 Hz		11.0, 10.7, 10.3, 9.8 mJ/cm²	Fiber	EC-12R (Alpinion Medical Systems)	Thyroid cancer
Yang et al. [46]	Linear	192	5.8 MHz		Handheld B-scan	1064 nm	10 Hz		5.5 mJ/cm²	Fiber	Resona7 (Mindray Bio-Medical Electronics Co. Ltd.)	Thyroid cancer
Irisawa et al. [30]	Linear	128	9 MHz		Motorized stage	750 nm	10 Hz	50 ± 10 ns	≤ 14.3 mJ/cm²	Fiber	FC1 (Fujifilm Medical Co. Ltd.)	Peripheral vasculature
Hai et al. [56]	Linear	256	21 MHz	78%	Stationary B-scan	850 nm	20 Hz		10 mJ/cm²	Fiber	Vevo LAZR (Visualsonics Inc.)	Vascualr compliance
Van den Berg et al. [31]	Linear	128	7.5 MHz	2.5–10 MHz	Stationary B-scan	808 nm	2 kHz	120 ns	3.2 mW/cm²	Free-space	MylabOne (ESAOTE Europe)	Finger
Jo et al. [32]	Linear		11.25 MHz		Handheld B-scan	576, 584 nm				Fiber	V1 (Verasonics)	Inflammatory arthritis
Dima et al. [47]	Concave	64	5 MHz		Handheld B-scan	800 nm	10 Hz	5 ns	≤ 20 mJ/cm²	Fiber	Custom ADC	Thyroid
Diot et al. [48]	Concave	256	5 MHz		Handheld B-scan	700–970 nm (10 nm step)	50 Hz	8 ns	≤ 15 mJ/pulse	Fiber	Custom ADC	Breast cancer
Taruttis et al. [29]	Concave	128	8 MHz		Handheld B-scan	730, 750, 800, 830 nm	10 Hz			Fiber	Custom ADC	Peripheral vasculature
Ermilov et al. [50]	Concave	128	5 MHz		Motorized stage	755 nm	10 Hz	75 ns	100 mJ/pulse	Fiber		Finger
Oeri et al. [49]	Concave	768	11–14 MHz	15 MHz	Motorized stage	700 nm	100 Hz	6 ns	2.9 mJ/cm²	Fiber	Custom ADC	Arthritis
Ishihara et al. [38]	Convex		6.5 MHz		Handheld B-scan	755 nm	10 Hz	40–50 ns	15 mJ/cm²	Fiber	Portable US system	Prostate, uterine cancer
Manohar et al. [72]	2D circular	588	1 MHz	130%	Stationary volumetric scan	1064 nm	10 Hz	10 ns		Free-space	NI PXI 5105 (National Instruments)	Breast cancer
Toi et al. [51]	2D hemisphere	512	2 MHz	70%	Motorized stage	755, 795 nm	10 Hz	75 ns	200 mJ/pulse	Free-space		Breast cancer
Dean-Ben et al. [44]	2D hemisphere	256	4 MHz	100%	Handheld volumetric scan	680–980 nm	10 Hz	< 10 ns		Fiber	Data acquisition cards	Melanoma

stainless steel slit at the focal line of the 1D transducer (Fig. 10b). They used a slit with the thickness of 4 times the acoustic wavelength to minimize the acoustic transmission. They demonstrated that the slit greatly diffracts the acoustic wave and increases the acoustic numerical aperture in the elevational direction. As a result, they improved the elevation resolution to 330 μm, which is close to the lateral resolution of 298 μm and enhanced the SNR by about four times [79, 80].

Unlike pulse-echo US signals, PA signals have a very broad bandwidth, ranging from 1 to 100 MHz [82]. However, the conventional piezoelectric (PZT) transducer cannot fully receive the PA signals resulting in the loss of sensitivity and spatial resolution. Recently, two alternative PA sensors have emerged to provide wide frequency bandwidth compared to the PZT transducer: Fabry–Perot (FP) interferometer and CMUT. FP interferometer is a US sensor that detects the reflected continuous wave laser modulated by the acoustic pressure. The FP sensor has a great advantage of being able to receive ultra-wideband signals. In addition, the FP sensor is optically transparent so that it can illuminate the object directly through the sensor without having to bypass the detector. Ansari et al. reported an FP sensor based endoscopic probe with 15-μm FP sensor thickness, 68 MHz − 3 dB bandwidth, and achieved very high lateral resolution of 57 μm at 1-mm depth [83]. Plumb et al. reported human peripheral vasculature imaging using a system based on FP sensor with 30-MHz − 3 dB bandwidth and a high spatial resolution of around 100 μm [81]. To accelerate the imaging speed, multiple beams [84] and subsampling reconstruction [85] are also be used. The CMUT probe has a wider bandwidth than PZT [86] and achieves higher acceptance angle due to the low directivity. The CMUT probe can be easily integrated with microelectronic circuits due to the easy micro-level fabrication [87]. Oeri et al. used CMUT arrays of 15 MHz bandwidth to image finger for detecting inflammatory arthritis [49].

4 Conclusion

PAI is a promising medical imaging technology used for assessing the progression of cancers, PAD, and inflammatory arthritis complementing the existing imaging modalities. In this paper, we reviewed several clinical PAI systems classified based upon the imaging probe used. The specifications of all reviewed systems are summarized in Table 1. While PAI systems have come a long way, there are still several challenges remaining as we discussed in this paper. To deal with these challenges, many groups are developing novel approaches regarding detector geometry and the acoustic sensor itself. In addition, most of the clinical PAI studies

discussed are still in feasibility test stage. In the future, for the PAI technology to penetrate deeply into the clinical world, its clinical efficacy must be demonstrated through large-scale clinical trials. Furthermore, the PAI systems must be made cost-effective to widen their appeal to the various medical facilities. With these aspects addressed, we believe that PAI technology could become an indispensable clinical tool for better patient care and bring a new paradigm in the medical device industries.

Compliance with ethical standards

Conflict of interest All authors declare to have no conflict of interests.

Human and animals rights This article does not contain any studies with human participants or animals performed by any of the authors.

Informed consent Not applicable.

References

1. Bell AG. The photophone. J Franklin Inst. 1880;110:237–48.
2. Valluru KS, Wilson KE, Willmann JK. Photoacoustic Imaging in oncology: translational preclinical and early clinical experience. Radiology. 2016;280:332–49.
3. Upputuri PK, Pramanik M. Recent advances toward preclinical and clinical translation of photoacoustic tomography: a review. J Biomed Opt. 2017;22:041006–041006.
4. Valluru KS, Willmann JK. Clinical photoacoustic imaging of cancer. Ultrasonography. 2016;35:267–80.
5. Cai X, Kim C, Pramanik M, Wang LV. Photoacoustic tomography of foreign bodies in soft biological tissue. J Biomed Opt. 2011;16:046017.
6. Zhang Y, Jeon M, Rich LJ, Hong H, Geng J, Zhang Y, Shi S, Barnhart TE, Alexandridis P, Huizinga JD. Non-invasive multimodal functional imaging of the intestine with frozen micellar naphthalocyanines. Nat Nanotechnol. 2014;9:631–8.
7. Jeon M, Kim C. Multimodal photoacoustic tomography. IEEE Trans Multimedia. 2013;15:975–82.
8. Lee C, Han S, Kim S, Jeon M, Jeon MY, Kim C, Kim J. Combined photoacoustic and optical coherence tomography using a single near-infrared supercontinuum laser source. Appl Opt. 2013;52:1824–8.
9. Kim JY, Lee C, Park K, Han S, Kim C. High-speed and high-SNR photoacoustic microscopy based on a galvanometer mirror in non-conducting liquid. Sci Rep. 2016;6:34803.
10. Park K, Kim JY, Lee C, Jeon S, Lim G, Kim C. Handheld photoacoustic microscopy probe. Sci Rep. 2017;7:13359.

11. Kim C, Favazza C, Wang LV. In vivo photoacoustic tomography of chemicals: high-resolution functional and molecular optical imaging at new depths. Chem Rev. 2010;110:2756–82.

12. Yapici MK, Kim C, Chang C-C, Jeon M, Guo Z, Cai X, Zou J, Wang LV. Parallel acoustic delay lines for photoacoustic tomography. J Biomed Opt. 2012;17:116019–116019.

13. Park J, Jeon S, Meng J, Song L, Lee JS, Kim C. Delay-multiply-and-sum-based synthetic aperture focusing in photoacoustic microscopy. J Biomed Opt. 2016;21:036010–036010.

14. Laskey W, Aspelin P, Davidson C, Rudnick M, Aubry P, Kumar S, Gietzen F, Wiemer M, D. S. Group. Nephrotoxicity of iodixanol versus iopamidol in patients with chronic kidney disease and diabetes mellitus undergoing coronary angiographic procedures. Am Heart J. 2009;158:822–8.

15. Mailloux LU, Napolitano B, Bellucci AG, Vernace M, Wilkes BM, Mossey RT. Renal vascular disease causing end-stage renal disease, incidence, clinical correlates, and outcomes: a 20-year clinical experience. Am J Kidney Dis. 1994;24:622–9.

16. Abuelo GJ. Diagnosing vascular causes of renal failure. Ann Intern Med. 1995;123:601–14.

17. Greenland P, Alpert JS, Beller GA, Benjamin EJ, Budoff MJ, Fayad ZA, Foster E, Hlatky MA, Hodgson JM, Kushner FG. 2010 ACCF/AHA guideline for assessment of cardiovascular risk in asymptomatic adults: a report of the American College of Cardiology Foundation/American Heart Association task force on practice guidelines developed in collaboration with the American Society of Echocardiography, American Society of Nuclear Cardiology, Society of Atherosclerosis Imaging and Prevention, Society for Cardiovascular Angiography and Interventions, Society of Cardiovascular Computed Tomography, and Society for Cardiovascular Magnetic Resonance. J Am Coll Cardiol. 2010;56:e50–103.

18. Maslov K, Zhang HF, Wang LV. Effects of wavelength-dependent fluence attenuation on the noninvasive photoacoustic imaging of hemoglobin oxygen saturation in subcutaneous vasculature in vivo. Inverse Prob. 2007;23:S113.

19. Zhang HF, Maslov K, Sivaramakrishnan M, Stoica G, Wang LV. Imaging of hemoglobin oxygen saturation variations in single vessels in vivo using photoacoustic microscopy. Appl Phys Lett. 2007;90:053901.

20. Jeon M, Kim J, Kim C. Multiplane spectroscopic whole-body photoacoustic imaging of small animals in vivo. Med Biol Eng Comput. 2016;54:283–94.

21. Park S, Lee C, Kim J, Kim C. Acoustic resolution photoacoustic microscopy. Biomed Eng Lett. 2014;4:213–22.

22. Lee C, Jeon M, Jeon MY, Kim J, Kim C. In vitro photoacoustic measurement of hemoglobin oxygen saturation using a single pulsed broadband supercontinuum laser source. Appl Opt. 2014;53:3884–9.

23. Ku G, Wang X, Xie X, Stoica G, Wang LV. Imaging of tumor angiogenesis in rat brains in vivo by photoacoustic tomography. Appl Opt. 2005;44:770–5.

24. Lao Y, Xing D, Yang S, Xiang L. Noninvasive photoacoustic imaging of the developing vasculature during early tumor growth. Phys Med Biol. 2008;53:4203.

25. Mehrmohammadi M, Yoon SJ, Yeager D, Emelianov SY. Photoacoustic imaging for cancer detection and staging. Curr Mol Imaging. 2013;2:89–105.

26. Lakshman M, Needles A. Screening and quantification of the tumor microenvironment with micro-ultrasound and photoacoustic imaging. Nat Methods. 2015;12.

27. Erpelding TN, Kim C, Pramanik M, Jankovic L, Maslov K, Guo Z, Margenthaler JA, Pashley MD, Wang LV. Sentinel lymph nodes in the rat: noninvasive photoacoustic and US imaging with a clinical US system. Radiology. 2010;256:102–10.

28. Akers WJ, Edwards WB, Kim C, Xu B, Erpelding TN, Wang LV, Achilefu S. Multimodal sentinel lymph node mapping with single-photon emission computed tomography (SPECT)/computed tomography (CT) and photoacoustic tomography. Transl Res. 2012;159:175–81.

29. Taruttis A, Timmermans AC, Wouters PC, Kacprowicz M, van Dam GM, Ntziachristos V. Optoacoustic imaging of human vasculature: feasibility by using a handheld probe. Radiology. 2016;281:256–63.

30. Irisawa K, Hirota K, Hashimoto A, Murakoshi D, Ishii H, Tada T, Wada T, Hayakawa T, Azuma R, Otani N, Itoh K, Ishihara M. Photoacoustic imaging system for peripheral small-vessel imaging based on clinical ultrasound technology. Proc SPIE. 2016;9708:970807.

31. van den Berg PJ, Daoudi K, Bernelot Moens HJ, Steenbergen W. Feasibility of photoacoustic/ultrasound imaging of synovitis in finger joints using a point-of-care system. Photoacoustics. 2017;8:8–14.

32. Jo J, Xu G, Marquardt A, Girish G, Wang X. Photoacoustic evaluation of human inflammatory arthritis in human joints. Proc. SPIE. 2017;10064:1006409.

33. Weidner N. Tumor angiogenesis: review of current applications in tumor prognostication. In: Seminars in diagnostic pathology; 1993. p. 302–13.

34. Brenchley P. Antagonising angiogenesis in rheumatoid arthritis. Ann Rheum Dis. 2001;60:71–4.

35. Hockel M, Vaupel P. Tumor hypoxia: definitions and current clinical, biologic, and molecular aspects. J Natl Cancer Inst. 2001;93:266–76.

36. Anderson JL, Halperin JL, Albert NM, Bozkurt B, Brindis RG, Curtis LH, DeMets D, Guyton RA, Hochman JS, Kovacs RJ. Management of patients with peripheral artery disease (compilation of 2005 and 2011 ACCF/AHA guideline recommendations). Circulation. 2013;127:1425–43.

37. Park S, Jang J, Kim J, Kim YS, Kim C. Real-time triple-modal photoacoustic, ultrasound, and magnetic resonance fusion imaging of humans. IEEE Trans Med Imaging. 2017;36:1912–21.

38. Ishihara M, Horiguchi A, Shinmoto H, Tsuda H, Irisawa K, Wada T, Asano T. Comparison of transrectal photoacoustic, Doppler, and magnetic resonance imaging for prostate cancer detection. Proc SPIE. 2016;9708:970852.

39. Guo Z, Li L, Wang LV. On the speckle-free nature of photoacoustic tomography. Med Phys. 2009;36:4084–8.

40. Jacques SL. Optical properties of biological tissues: a review. Phys Med Biol. 2013;58:R37.

41. Kim C, Erpelding TN, Jankovic L, Pashley MD, Wang LV. Deeply penetrating in vivo photoacoustic imaging using a clinical ultrasound array system. Biomed Opt Exp. 2010;1:278–84.

42. Kang J, Zhang HK, Rahmim A, Wong DF, Kang JU, Boctor EM. Toward high-speed transcranial photoacoustic imaging using compact near-infrared pulsed LED illumination system. In: Photons plus ultrasound: imaging and sensing; 2017. p. 100643B.

43. Deán-Ben XL, Razansky D. On the link between the speckle free nature of optoacoustics and visibility of structures in limited-view tomography. Photoacoustics. 2016;4:133–40.

44. Deán-Ben XL, Razansky D. Functional optoacoustic human angiography with handheld video rate three dimensional scanner. Photoacoustics. 2013;1:68–73.

45. Kim J, Park S, Jung Y, Chang S, Park J, Zhang Y, Lovell JF, Kim C. Programmable real-time clinical photoacoustic and ultrasound imaging system. Sci Rep. 2016;6:35137.

46. Yang M, Zhao L, He X, Su N, Zhao C, Tang H, Hong T, Li W, Yang F, Lin L. Photoacoustic/ultrasound dual imaging of human thyroid cancers: an initial clinical study. Biomed Opt Exp. 2017;8:3449–57.

47. Dima A, Ntziachristos V. Non-invasive carotid imaging using optoacoustic tomography. Opt Exp. 2012;20:25044–57.

48. Diot G, Metz S, Noske A, Liapis E, Schroeder B, Ovsepian SV, Meier R, Rummeny E, Ntziachristos V. Multispectral optoacoustic tomography (MSOT) of human breast cancer. Clin Cancer Res. 2017;23:6912–22.

49. Oeri M, Bost W, Sénégond N, Tretbar S, Fournelle M. Hybrid photoacoustic/ultrasound tomograph for real-time finger imaging. Ultrasound Med Biol. 2017;43:2200–12.

50. Ermilov S, Su R, Zamora M, Hernandez T, Nadvoretsky V, Oraevsky A. Optoacoustic angiography of peripheral vasculature. In: Proceedings of SPIE; 2012. p. 82230D.

51. Toi M, Asao Y, Matsumoto Y, Sekiguchi H, Yoshikawa A, Takada M, Kataoka M, Endo T, Kawaguchi-Sakita N, Kawashima M, Fakhrejahani E, Kanao S, Yamaga I, Nakayama Y, Tokiwa M, Torii M, Yagi T, Sakurai T, Togashi K, Shiina T. Visualization of tumor-related blood vessels in human breast by photoacoustic imaging system with a hemispherical detector array. Sci Rep. 2017;7:41970.

52. Szabo TL, Lewin PA. Ultrasound transducer selection in clinical imaging practice. J Ultrasound Med. 2013;32:573–82.

53. Garcia-Uribe A, Erpelding TN, Krumholz A, Ke H, Maslov K, Appleton C, Margenthaler JA, Wang LV. Dual-modality photoacoustic and ultrasound imaging system for noninvasive sentinel lymph node detection in patients with breast cancer. Sci Rep. 2015;5:15748.

54. Neuschler EI, Butler R, Young CA, Barke LD, Bertrand ML, Böhm-Vélez M, Destounis S, Donlan P, Grobmyer SR, Katzen J. A pivotal study of optoacoustic imaging to diagnose benign and malignant breast masses: a new evaluation tool for radiologists. Radiology. 2017; 172228.

55. Kim J, Kim M-H, Jo K, Ha J, Kim Y, Lim D-J, Kim C. Photoacoustic analysis of thyroid cancer in vivo: a pilot study. In: Proceedings of SPIE; 2017. p. 1006470-1.

56. Hai P, Zhou Y, Liang J, Li C, Wang LV. Photoacoustic tomography of vascular compliance in humans. J Biomed Opt. 2015;20:126008.

57. Butler R, Stavros A, Lavin P, Ulissey M, Tucker F. Opto-acoustic breast imaging: imaging-pathology correlation of opto-acoustic features respecting malignancy; 2015.

58. Ermilov SA, Fronheiser MP, Brecht H-P, Su R, Conjusteau A, Mehta K, Otto P, Oraevsky AA. Development of laser optoacoustic and ultrasonic imaging system for breast cancer utilizing handheld array probes. In: SPIE BiOS; 2009. p. 10.

59. Ishihara M, Tsujita K, Horiguchi K, Irisawa K, Komatsu T, Ayaori M, Hirasawa T, Kasamatsu T, Hirota K, Tsuda H. Development of photoacoustic imaging technology overlaid on ultrasound imaging and its clinical application. In: SPIE BiOS; 2015. p. 93232K–93232K-7.

60. Hai P, Zhou Y, Gong L, Wang LV. Quantitative photoacoustic elastography in humans. J Biomed Opt. 2016;21:5.

61. Daoudi K, van den Berg PJ, Rabot O, Kohl A, Tisserand S, Brands P, Steenbergen W. Handheld probe integrating laser diode and ultrasound transducer array for ultrasound/photoacoustic dual modality imaging. Opt Exp. 2014;22:26365–74.

62. Xu G, Rajian JR, Girish G, Kaplan MJ, Fowlkes JB, Carson PL, Wang X. Photoacoustic and ultrasound dual-modality imaging of human peripheral joints. J Biomed Opt. 2013;18:010502.

63. Yuan J, Xu G, Yu Y, Zhou Y, Carson PL, Wang X, Liu X. Real-time photoacoustic and ultrasound dual-modality imaging system facilitated with graphics processing unit and code parallel optimization. J Biomed Opt. 2013;18:086001.

64. Dima A, Ntziachristos V. In-vivo handheld optoacoustic tomography of the human thyroid. Photoacoustics. 2016;4:65–9.

65. Okawa S, Sei K, Hirasawa T, Irisawa K, Hirota K, Wada T, Kushibiki T, Furuya K, Ishihara M. In vivo photoacoustic imaging of uterine cervical lesion and its image processing based on light propagation in biological medium. Proc SPIE. 2017;10064:100642S.

66. Buehler A, Kacprowicz M, Taruttis A, Ntziachristos V. Real-time handheld multispectral optoacoustic imaging. Opt Lett. 2013;38:1404–6.

67. Rosenthal A, Razansky D, Ntziachristos V. Fast semi-analytical model-based acoustic inversion for quantitative optoacoustic tomography. IEEE Trans Med Imaging. 2010;29:1275–85.

68. Glatz J, Deliolanis NC, Buehler A, Razansky D, Ntziachristos V. Blind source unmixing in multi-spectral optoacoustic tomography. Opt Express. 2011;19:3175–84.

69. Taruttis A, Rosenthal A, Kacprowicz M, Burton NC, Ntziachristos V. Multiscale multispectral optoacoustic tomography by a stationary wavelet transform prior to unmixing. IEEE Trans Med Imaging. 2014;33:1194–202.

70. Brecht H-P, Su R, Fronheiser M, Ermilov SA, Conjusteau A, Oraevsky AA. Whole-body three-dimensional optoacoustic tomography system for small animals. J Biomed Opt. 2009;14:064007.

71. Heijblom M, Steenbergen W, Manohar S. Clinical photoacoustic breast imaging: the Twente experience. IEEE Pulse. 2015;6:42–6.

72. Manohar S, Kharine A, van Hespen JC, Steenbergen W, van Leeuwen TG. The twente photoacoustic mammoscope: system overview and performance. Phys Med Biol. 2005;50:2543.

73. Heijblom M, Piras D, Brinkhuis M, van Hespen JCG, van den Engh FM, van der Schaaf M, Klaase JM, van Leeuwen TG, Steenbergen W, Manohar S. Photoacoustic image patterns of breast carcinoma and comparisons with Magnetic resonance Imaging and vascular stained histopathology. Sci Rep. 2015;5:11778.

74. Kruger RA, Kuzmiak CM, Lam RB, Reinecke DR, Del Rio SP, Steed D. Dedicated 3D photoacoustic breast imaging. Med Phys. 2013;40:113301.

75. Chuah S, Attia A, Long V, Ho C, Malempati P, Fu C, Ford S, Lee J, Tan W, Razansky D. Structural and functional 3D mapping of skin tumours with non-invasive multispectral optoacoustic tomography. Skin Res Technol. 2017;23:221–6.

76. Deán-Ben X, Merčep E, Razansky D. Hybrid-array-based optoacoustic and ultrasound (OPUS) imaging of biological tissues. Appl Phys Lett. 2017;110:203703.

77. Gateau J, Gesnik M, Chassot J-M, Bossy E. Single-side access, isotropic resolution, and multispectral three-dimensional photoacoustic imaging with rotate-translate scanning of ultrasonic detector array. J Biomed Opt. 2015;20:056004-1.

78. Schwarz M, Buehler A, Ntziachristos V. Isotropic high resolution optoacoustic imaging with linear detector arrays in bi-directional scanning. J Biophotonics. 2015;8:60–70.

79. Wang Y, Wang D, Zhang Y, Geng J, Lovell JF, Xia J. Slit-enabled linear-array photoacoustic tomography with near isotropic spatial resolution in three dimensions. Opt Lett. 2016;41:127–30.

80. Wang Y, Wang D, Hubbell R, Xia J. Second generation slit-based photoacoustic tomography system for vascular imaging in human. J Biophotonics. 2017;10:799–804.

81. Plumb AA, Huynh NT, Guggenheim J, Zhang E, Beard P. Rapid volumetric photoacoustic tomographic imaging with a Fabry-Perot ultrasound sensor depicts peripheral arteries and microvascular vasomotor responses to thermal stimuli. Eur Radiol 2017; 1–9.

82. Vallet M, Varray F, Kalkhoran MA, Vray D, Boutet J. Enhancement of photoacoustic imaging quality by using CMUT technology: experimental study. In: 2014 IEEE International ultrasonics symposium (IUS); 2014. p. 1296–99.

83. Ansari R, Zhang E, Desjardins AE, Beard PC. All-optical endoscopic probe for high resolution 3D photoacoustic tomography. Proc SPIE. 2017;10064:100641W.

84. Huynh N, Ogunlade O, Zhang E, Cox B, Beard P. Photoacoustic imaging using an 8-beam Fabry-Perot scanner. Proc. SPIE. 2016;9708:97082L.

85. Huynh N, Lucka F, Zhang E, Betcke M, Arridge S, Beard P, Cox B. Sub-sampled Fabry-Perot photoacoustic scanner for fast 3D imaging. Proc SPIE. 2017;10064:100641Y.

86. Vallet M, Varray F, Boutet J, Dinten J-M, Caliano G, Savoia AS, Vray D. Quantitative comparison of PZT and CMUT probes for photoacoustic imaging: experimental validation. Photoacoustics. 2017;8:48–58.

87. Warshavski O, Meynier C, Sénégond N, Chatain P, Rebling J, Razansky D, Felix N, Nguyen-Dinh A. Experimental evaluation of cMUT and PZT transducers in receive only mode for photoacoustic imaging. In: Proceedings of SPIE; 2016. p. 970830.